

Electronic Supporting Information

Support Stabilized PtCu Single-atom Alloys for Propane Dehydrogenation

5

Xiaohe Liu, Xianhui Wang, Shiyu Zhen, Guodong Sun, Chunlei Pei, Zhi-Jian Zhao,
and Jinlong Gong*

10 *Key Laboratory for Green Chemical Technology of Ministry of Education, School of
Chemical Engineering and Technology, Tianjin University; Collaborative Innovation
Center of Chemical Science and Engineering, Tianjin 300072, China;*

*Corresponding authors: jlgong@tju.edu.cn

15

Contents

S1. Experimental and computational methods

S2. Supporting figures and tables

S3. Reference

S1. Experimental and computational methods

1.1 Chemicals and Materials

All chemicals were used as received without further purification. Amorphous silica (300 m²/g, particle size 7-40 nm, 99.8% metals basis), Cu(NO₃)₂·3H₂O (99.99% metals basis) and ammonium hydroxide (GR, 25-28%) were purchased from Aladdin. H₂PtCl₆·6H₂O (99.9%) was purchased from Chemart (Tianjin) Chemical Technology Co., Ltd. All aqueous solutions were prepared with ultra-purity water (18.25 MΩ·cm) supplied by the Merck Milli-Q Direct Q5 system. C₃H₈, H₂, N₂ and Ar were supplied by Air Liquid (≥99.999%).

10 1.2 Preparation of Copper phyllosilicate support

Copper phyllosilicate support with lamellar structure was prepared by an ammonia evaporation hydrothermal method (AEM) described briefly as follows^{1, 2}. A certain amount of Cu(NO₃)₂·3H₂O, adjusted to yield 7 wt.% of Cu in the final catalysts, dissolved in 10mL deionized water mixed with 25 wt.% ammonia aqueous solution (the molar ratio of NH₃⁺/Cu²⁺ is 8) and stirred for 15 minutes to obtain the copper ammonia complex solution with the color of ultramarine. Subsequently, 5g of amorphous silica was dispersed in 165mL deionized water under vigorously stirring for 30 minutes to ensure that the silica was wholly dispersed to form silica solution. And then, the copper ammonia complex solution was added dropwise into the above solution, followed by adjusting the initial pH of the suspension to 11-12. All the above operations were performed at room temperature. The suspension was heated in a water bath preheated to 80 °C to allow for the evaporation of ammonia and the consequent deposition of copper species on silica. When the pH value of the suspension decreased to 6-7, the evaporation process was terminated. Then the sol was hydrothermally treated at 190 °C for 20 hours. The resultant precipitate was filtered and washed thoroughly by deionized water to remove the residual ammonium ions. Then, the solid was dried at 80 °C for 12 hours in a drying oven and was calcined at 550 °C for 4 hours in a muffle furnace with the heating rate is 5 °C/min.

1.3 Preparation of 0.1Pt/7CuSiO₃ and 0.1Pt7Cu/SiO₂-IM catalysts

The incipient wetness impregnation method was used to synthesize 0.1Pt/7CuSiO₃ with 0.1 wt.% Pt precursor loading. The reference catalysts 0.1Pt7Cu/SiO₂-IM were prepared by the co-impregnation method typically with the same loading of Pt precursor and Cu precursor in order to a fair comparison. Then, the slurry was dried at 80 °C for 12 hours in a drying oven before hydrogen reduction treatment.

1.4 Characterization methods

To determine the morphology of the size of Cu NPs in catalysts, transmission electron microscope (TEM) and HAADF-STEM were obtained by using a JEOL JEM-F200 Field Emission Transmission Electron Microscope equipped with energy dispersive X-ray spectrometer (EDX) measurements operated at an accelerating voltage of 200 kV. For the catalysts of 0.1Pt7Cu/SiO₂-IM and 0.1Pt7CuSiO₃, the sample was reduced at 580/680/780 °C for 1 hour in a stream of 10 vol% H₂/He with the heating rate is 10 °C/min. Then, the sample powder was dispersed in deionized water and supported on a molybdenum grid coated with an ultrathin holey carbon film.

Aberration-corrected high-angle annular dark-field scanning transmission electron microscopy (AC-HAADF-STEM) images were collected using a JEM-ARM200F 200 kV aberration-corrected scanning transmission electron microscope capable of sub-angstrom resolution at School of Materials Science and Engineering, Tianjin University. For the catalysts of 0.1Pt7CuSiO₃-680R, the sample was first reduced at 680 °C for 1 hour in a stream of 10 vol% H₂/He. Then, the sample powder was dispersed in deionized water by ultrasonic and deposited on a copper grid coated with an ultrathin holey carbon film.

The in situ diffuse reflectance infrared Fourier-transform spectroscopy (DRIFTS) experiments were performed on a Thermo Scientific Nicolet IS50 spectrometer, equipped with a Harrick Scientific DRIFTS cell fitted with ZnSe windows and a mercury-cadmium-telluride (MCT) detector cooled by liquid nitrogen. The CO-DRIFTS experiments were carried out for catalysts with different pretreatment temperatures. The fresh catalysts were heated from ambient temperature to

580/630/680/730/780 °C at a rate of 10 °C·min⁻¹ and retained at a relevant temperature at a flow rate of 30 mL min⁻¹ of 10 vol% H₂/Ar for 1 h. Then, the catalysts were cooled down to 30 °C, and the backgrounds (4 cm⁻¹ resolution, 64 scans) were collected after Ar purging in a flow rate of 20 mL min⁻¹ for at least 1h until the background is unchangeable. With the addition of a flow of 3 mL min⁻¹ of CO, the adsorption of CO molecules on the surface of the catalysts continued for 30 min. After that, the CO desorption DRIFTS spectra were continuous recorded till no visible change in the absorption band intensities under Ar purging.

In situ XRD measurements were performed on a Rigaku Smartlab diffractometer operating at 200 mA and 40 kV, employing the graphite filtered Cu K α as the radiation source. The data points were collected by step scanning with a rate of 10° min⁻¹ from 10° to 80° (2 θ). The crystallite size (D) of copper was calculated by X-ray broadening technique using Scherrer's equation:

$$D = \frac{K \cdot \lambda}{\beta \cdot \cos\theta}$$

Here, K is the Scherrer constant (0.9); λ is the wavelength of the radiation source (0.15406 nm); β is the half-width of the most substantial diffraction peak in the radian unit; and θ is its diffraction angle.

Quasi-in situ XPS analysis has been performed in Thermo Fischer ESCALAB 250Xi photoelectron spectrometer using mono-chromated X-ray irradiation Al K α ($h\nu= 1486.7$ eV) and 180° double-focusing hemispherical analyzer with a six-channel detector. The binding energy (BE) of the photoemission spectra was calibrated with the adventitious carbon signal centered at 284.8 eV. Reduction of samples was performed in a UHV connected high-pressure gas cell. The samples were heated in 10% hydrogen diluted with Ar flow (1 mL/min H₂ and 9 mL/min Ar, total pressure 1 bar) to corresponding temperature followed by holding 60 min. The photoelectron spectra were recorded under the UHV after transferring the samples to the analyzer chamber without contact with the atmosphere.

In situ Raman patterns were recorded using a Renishaw inVia reflex Raman spectrometer with a 325 nm He-Cd laser beam. Samples were pretreated at

corresponding temperature followed by holding 60 min for 1h in 10% hydrogen diluted with Ar flow (1 mL/min H₂ and 9 mL/min Ar, total pressure 1 bar).

1.5 Catalytic Propane Dehydrogenation Reaction Test

Catalytic tests were performed in a quartz fixed-bed reactor with an 8 mm inner diameter and 24 cm length at atmosphere pressure. 200 mg of catalyst precursors with a particle size of 20 to 40 meshes was packed inside the quartz tubular reactor. The sample was first heated to predetermined reduction temperature at a rate of 15°C min⁻¹ and retained at that temperature for 1 h in flowing 10 vol.% H₂/N₂, followed by cooling down to the reaction temperature. During the activity test, a mixture of C₃H₈ (Air Liquide, 99.9%), H₂ (Air Liquide, 99.9%), and N₂ (Air Liquide, 99.9%) (14:14:72 vol %) was fed at a rate of 50 mL min⁻¹ over 200 mg catalysts. The WHSV of propane was around 4.7 h⁻¹. The gas products were analyzed by an online GC (2060) equipped with a flame ionization detector (chromosorb 102 column) and a thermal conductivity detector (Al₂O₃ plot column). The propane conversion and selectivity to propylene were calculated from Equation 1 and 2, respectively. The propylene productivity is defined as the moles of C₃H₆ formation per g Pt per hour from Equation 3:

$$Con(\%) = 100 \times ([F_{C_3H_8}]_{inlet} - [F_{C_3H_8}]_{outlet})/[F_{C_3H_8}]_{inlet} \quad (\text{Equation 1})$$

$$Sel(\%) = 100 \times [F_{C_3H_6}]_{outlet}/([F_{C_3H_8}]_{inlet} - [F_{C_3H_8}]_{outlet}) \quad (\text{Equation 2})$$

$$productivity = [F_{C_3H_6}]_{outlet}/(22.4 \cdot m_{cat} \cdot w_{Pt}) \quad (\text{Equation 3})$$

where $[F_{C_3H_8}]$ and $[F_{C_3H_6}]$ mean mole flow rate of propane and propylene. m_{cat} is the weight of catalysts, and w_{Pt} is the weight percent of Pt supported on the sample.

A first-order deactivation model was used to evaluate the catalyst stability:

$$k_d = (\ln[(1 - X_{final})/X_{final}] - \ln[(1 - X_{initial})/X_{initial}])/t \quad (\text{Equation 4})$$

Where $X_{initial}$ and X_{final} , respectively, represent the conversion measured at the initial and final period of an experiment, and t represents the reaction time (h), k_d is the deactivation rate constant (h⁻¹). A high k_d value means rapid deactivation, that is, low stability.

1.6 Computational methods

Density functional theory (DFT) calculation were performed with the plane-wave-based Vienna Ab Initio Simulation package, VASP.³ The electron exchange and adsorbate interactions were described by the generalized gradient approximation (GGA) in the form of the Bayesian error estimation functional with van der Waals correlation (BEEF-vdW),^{4,5} which was considered an effective method for describing interactions between adsorbates and surfaces. The projector augmented wave (PAW) method was used to describe the interaction between the atomic cores and electrons.⁶ In this study, Cu⁰ terrace sites, Cu⁰ step sites and Cu⁺ step sites were represent by a four-layer Cu(111)-(3×3) slab, a four-layer Cu(321)-(3×3) slab, a four-layer Cu(211)-(3×3) slab and a four-layer Cu₂O(111)-(2×2), respectively. For Cu₂O, we used DFT+U theory to describe the localized 3d electrons in copper, where $U_{\text{Cu}} - J_{\text{Cu}} = 4.0$ eV was adopted.⁷ A K-points set of 3×3×1 was applied in all calculations after the convergence test. Four layers were used for above models, where the two bottom layers were kept fixed in optimization. The optimization calculations were employed with a plane-wave cutoff energy of 400 eV and an atomic force convergence of 0.02 eV/Å. The slab was separated from its periodic images in the vertical direction by a vacuum space with at least 15 Å.

S2 Supplemental Figures and Tables

2.1 Supporting figures

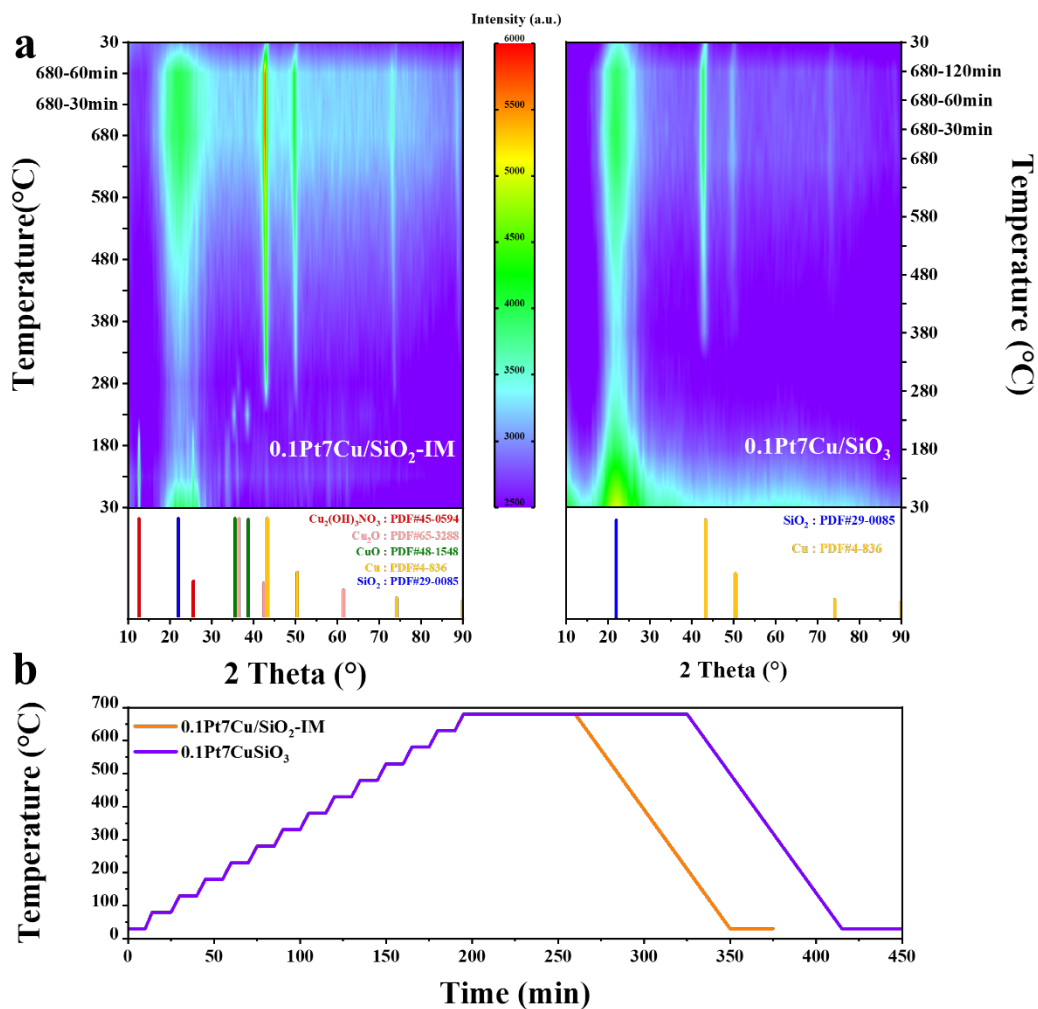


Figure S1. (a) *In situ* XRD patterns of 0.1Pt7Cu/SiO₂-IM and 0.1Pt7Cu/SiO₃ under reductive atmosphere. (b) Procedure for *in situ* XRD during H₂ reduction.

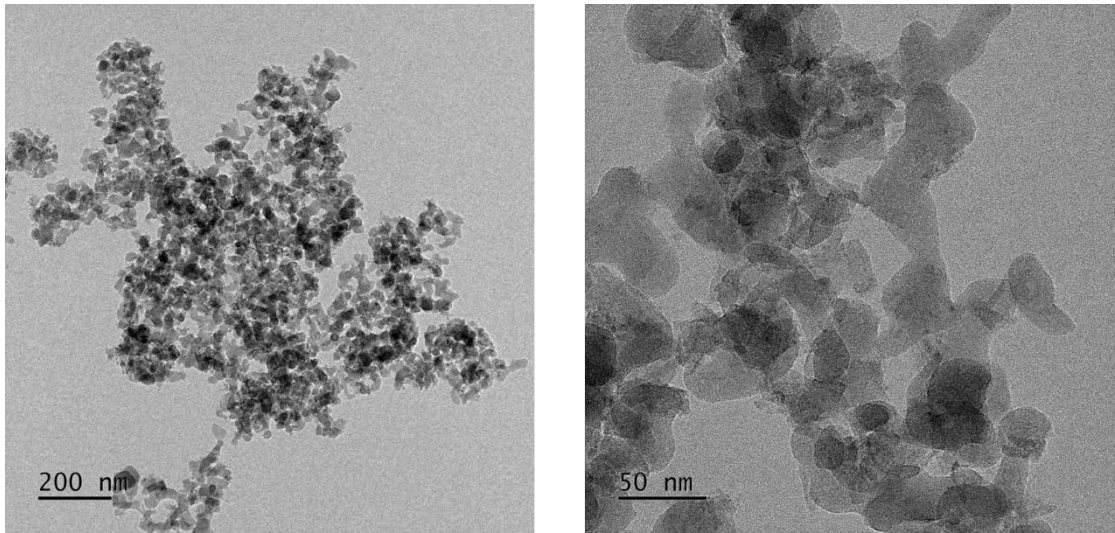


Figure S2. Typical TEM images of $0.1\text{Pt}7\text{CuSiO}_3$ before reduction.

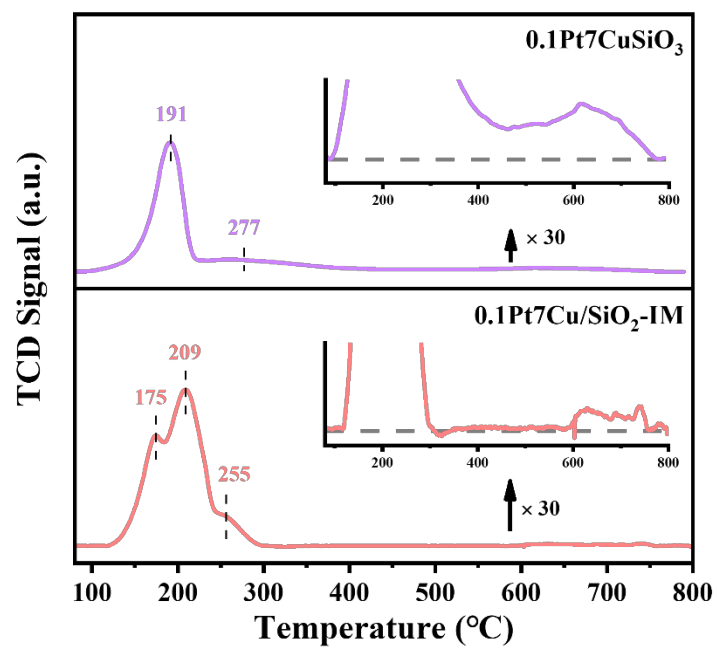


Figure S3. Temperature-programmed reduction (TPR) profiles of 0.1Pt7Cu/SiO₂-IM and 0.1Pt7CuSiO₃.

5

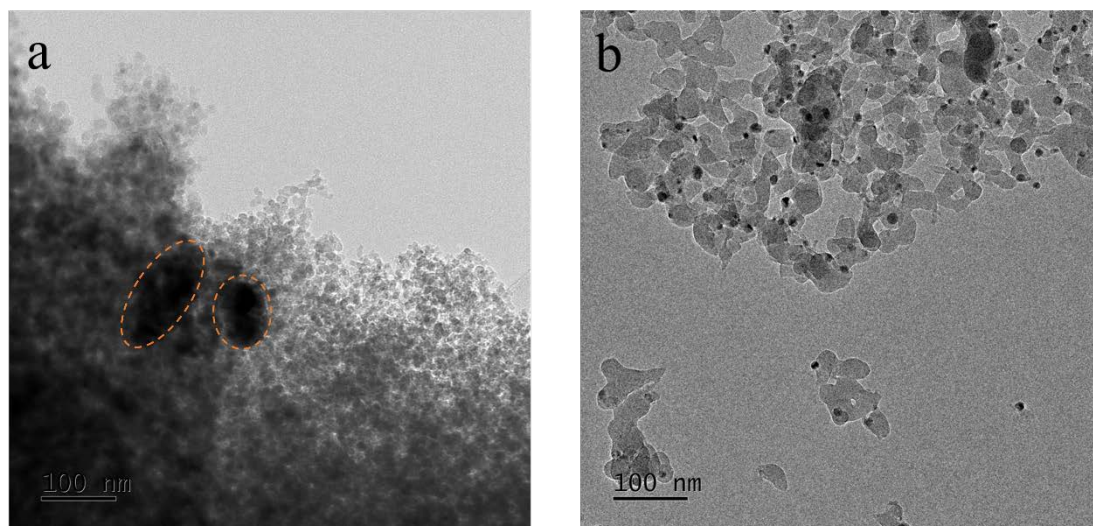


Figure S4. Typical TEM images of (a) 0.1Pt7Cu/SiO₂-IM-680R, (b) 0.1Pt7CuSiO₃-680R. The sintered Cu NP is highlighted by orange dotted circle.

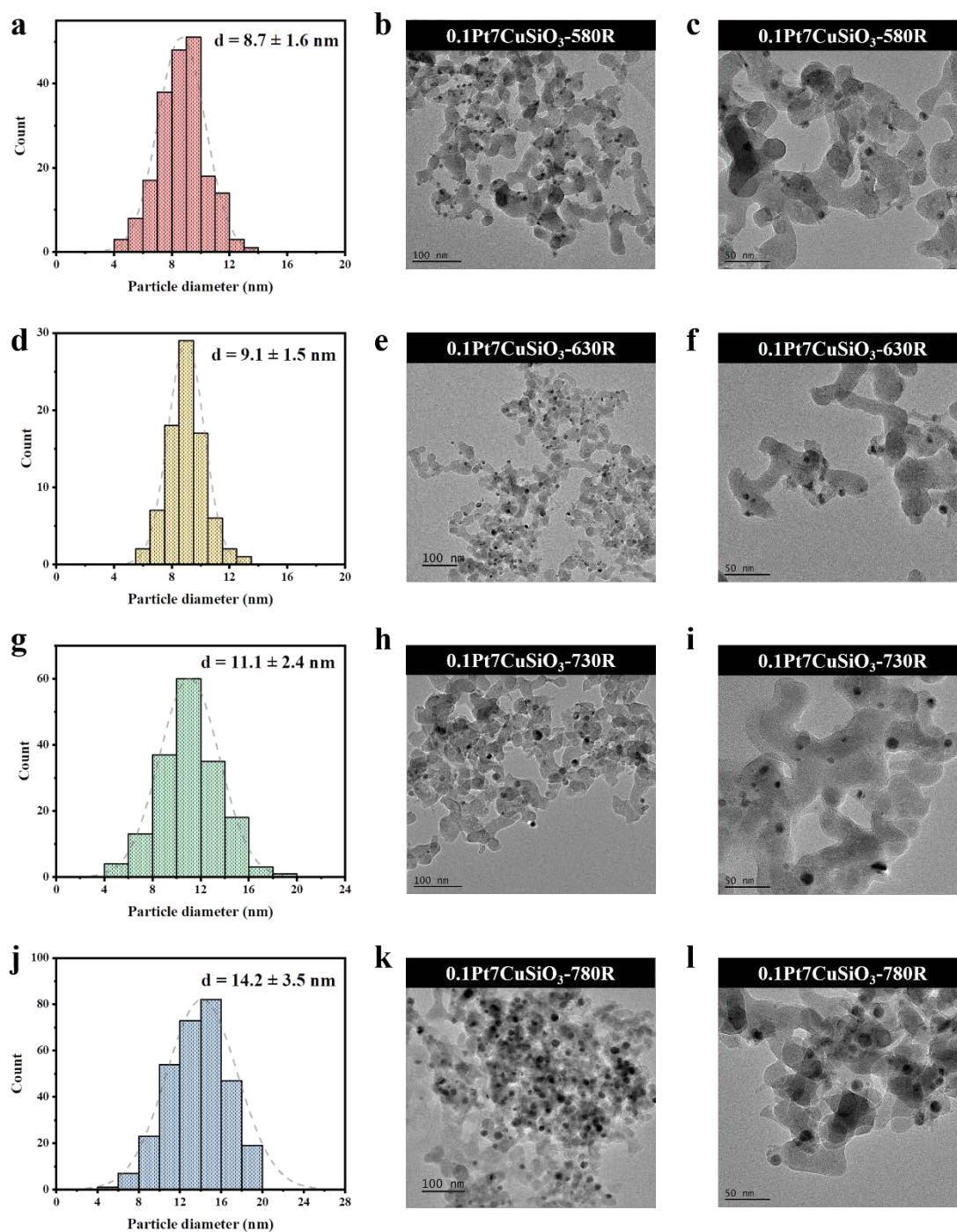


Figure S5. Typical TEM images and particle size distributions of (a, b, c) $0.1\text{Pt}_7\text{CuSiO}_3$ -580R, (d, e, f) $0.1\text{Pt}_7\text{CuSiO}_3$ -630R, (g, h, i) $0.1\text{Pt}_7\text{CuSiO}_3$ -730R, (j, k, l) $0.1\text{Pt}_7\text{CuSiO}_3$ -780R.

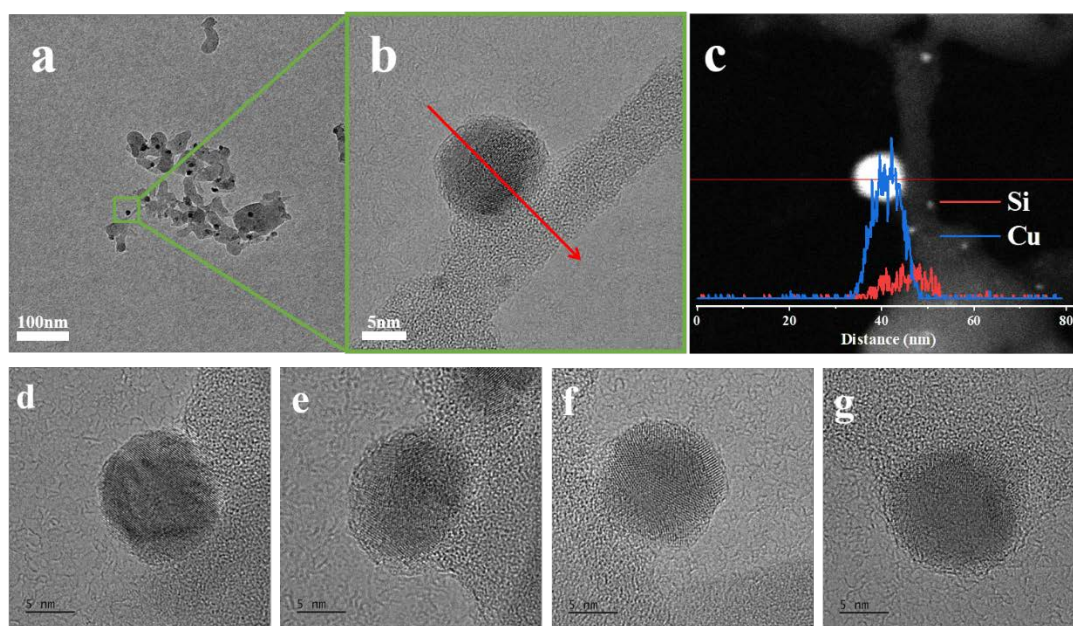


Figure S6. (a, b) Representative TEM images of 0.1Pt7CuSiO₃-680R. (c) Corresponding HAADF-STEM images include line scan of Cu nanoparticle. (d-g) Representative TEM images of 0.1Pt7CuSiO₃-680R.

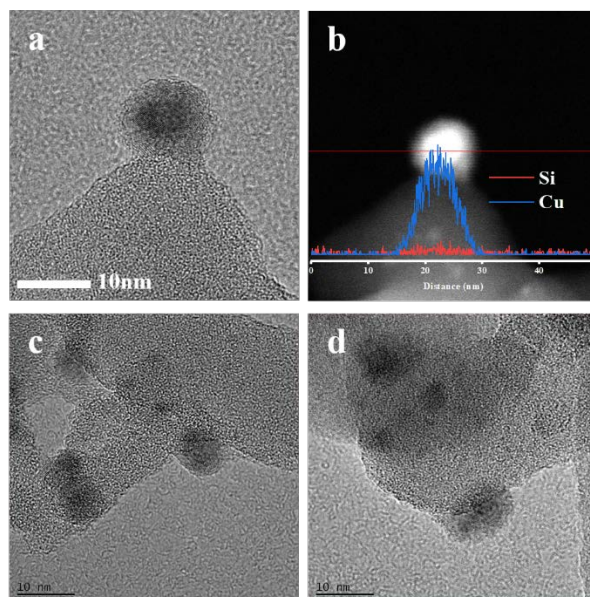


Figure S7. (a) Representative TEM images of 0.1Pt7CuSiO₃-580R. (b) Corresponding HAADF-STEM images include line scan of Cu nanoparticle. (c, d) Representative TEM images of 0.1Pt7CuSiO₃-580R.

5

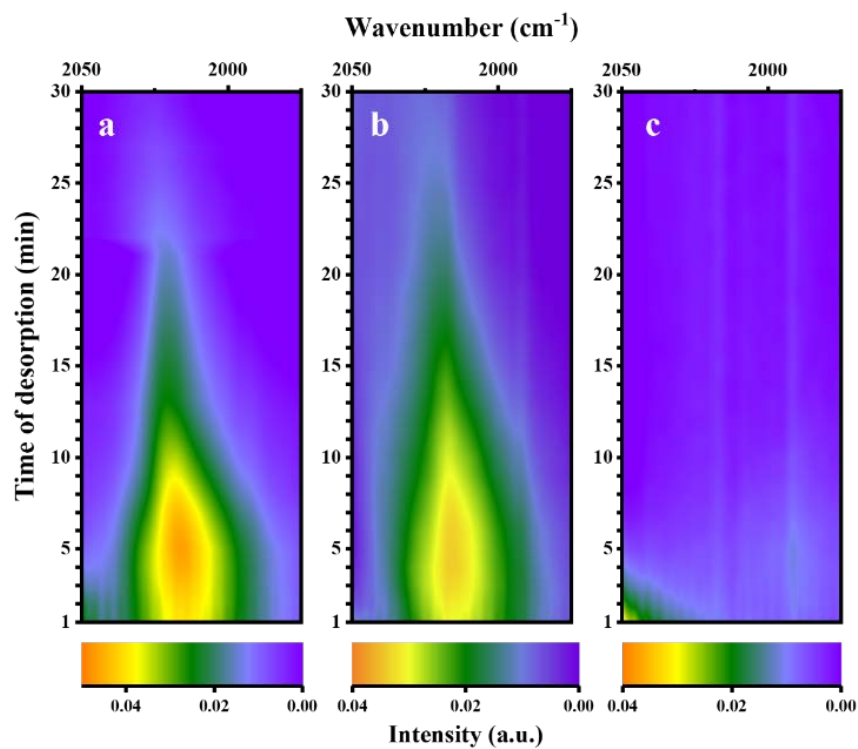


Figure S8. Time-dependent desorption infrared spectra recorded after exposing the 0.1Pt7CuSiO₃ catalysts reduction under different temperature to CO at room temperature and subsequently desorption by pure Ar flow: (a) 0.1Pt7CuSiO₃-580R; (b) 0.1Pt7CuSiO₃-680R; (c) 5 0.1Pt7CuSiO₃-780R.

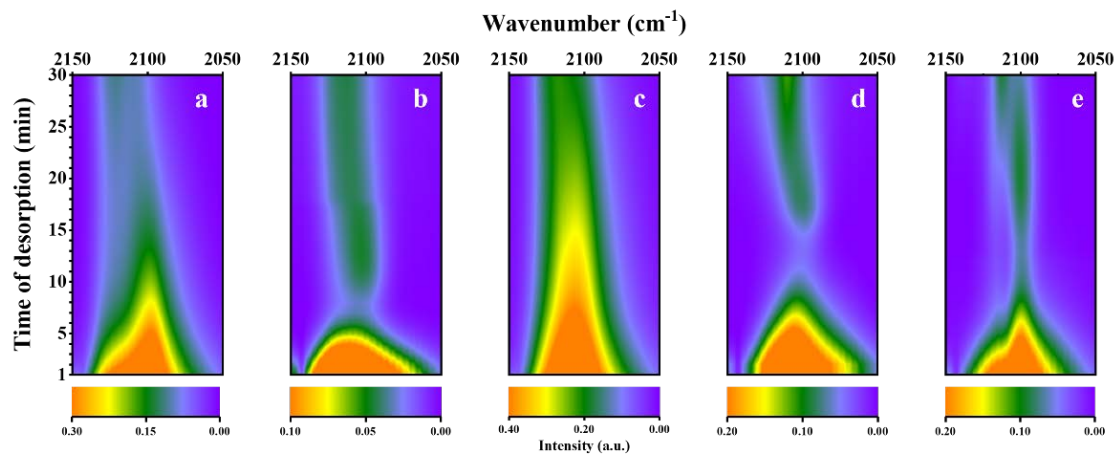


Figure S9. Time-dependent desorption infrared spectra recorded after exposing the 0.1Pt7CuSiO₃ catalysts reduction under different temperatures to CO at room temperature and subsequently desorption by pure Ar flow: (a) 0.1Pt7CuSiO₃-580R; (b) 0.1Pt7CuSiO₃-630R; (c) 5 0.1Pt7CuSiO₃-680R; (d) 0.1Pt7CuSiO₃-730R; (e) 0.1Pt7CuSiO₃-780R.

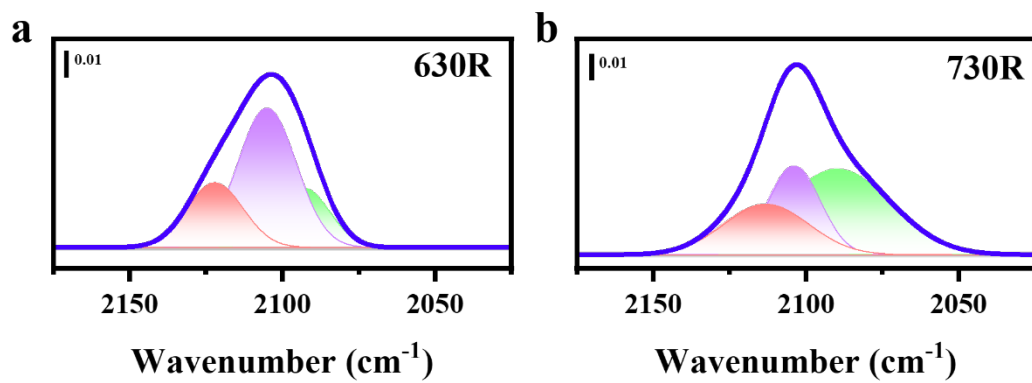


Figure S10. CO-DRIFTS spectra of (a) 0.1Pt7CuSiO₃-630R and (b) 0.1Pt7CuSiO₃-730R.

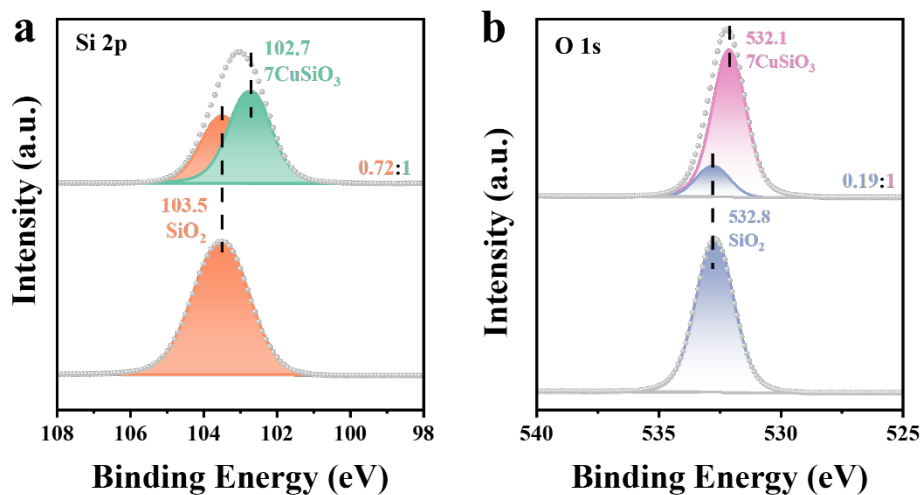


Figure S11. (a) Si 2p and (b) O 1s XPS spectrum of fresh 0.1Pt7CuSiO₃ and SiO₂.

Compared with pure SiO₂, the binding energy of Si 2p and O 2p in fresh 0.1Pt7CuSiO₃ obviously shifted towards lower binding energy due to the electrons of Cu²⁺ species shift towards Si-O moieties.⁸

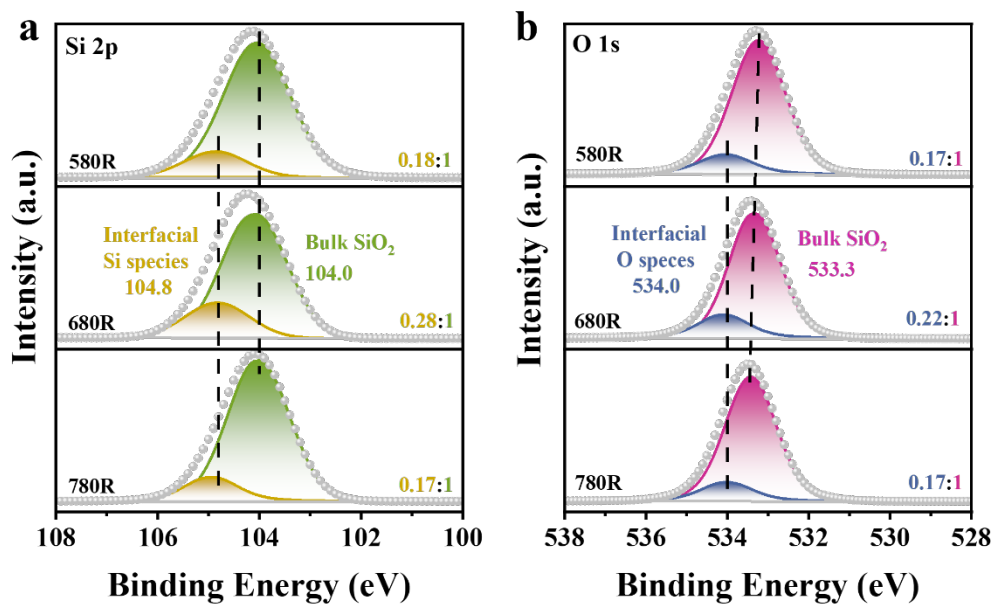


Figure S12. (a) Si 2p and (b) O 1s XPS spectrum of 0.1Pt7CuSiO₃-580R, 0.1Pt7CuSiO₃-680R and 0.1Pt7CuSiO₃-780R.

After high-temperature reduction, the binding energy of the interfacial species (Si and O) shifted towards higher binding energy due to the decreasing of the electron density of Si and O, which indicate Cu⁺-O-Si species .^{8,9}

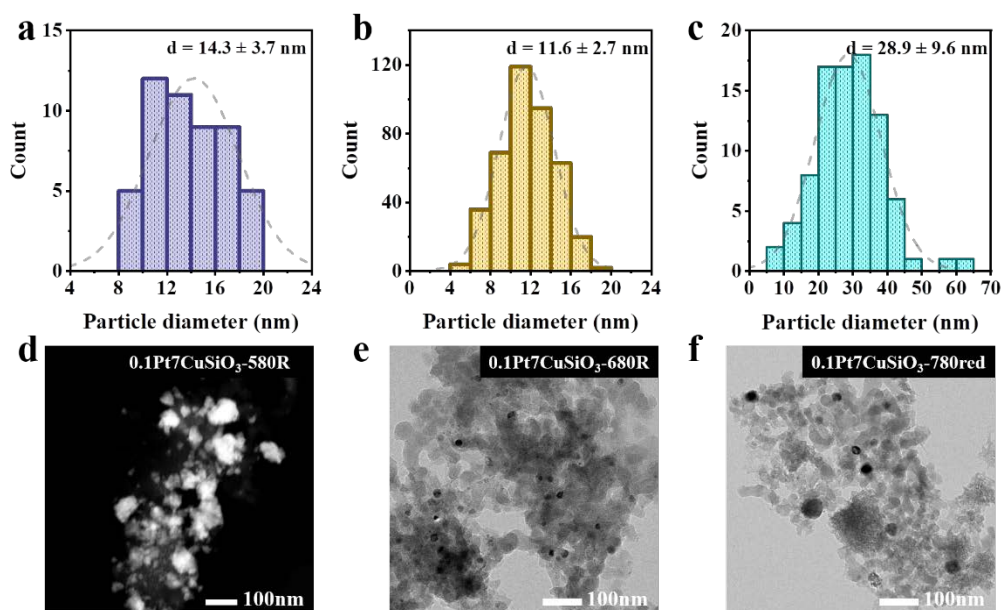


Figure S13. Typical TEM images and particle size distributions of (a, d) $0.1\text{Pt}7\text{CuSiO}_3\text{-580R}$, (b, e) $0.1\text{Pt}7\text{CuSiO}_3\text{-680R}$, (c, f) $0.1\text{Pt}7\text{CuSiO}_3\text{-780R}$ after 6 h PDH reaction.

The HAADF-STEM image of spent $0.1\text{Pt}7\text{CuSiO}_3\text{-580R}$ sample showed that the vigorous sintering of Cu happened due to the lack of $\text{Cu}^+\text{-O-Si}$ species to stabilize Cu NPs. So, we only counted for the un-sintered Cu NPs. The particle size of $0.1\text{Pt}7\text{CuSiO}_3\text{-780R}$ had significantly increased from 14.2 nm to 28.9 nm (increased by 100%) after 6 h PDH reaction, whereas, the phenomenon of large-scale sintering like $0.1\text{Pt}7\text{CuSiO}_3\text{-580R}$ sample was absence.

10

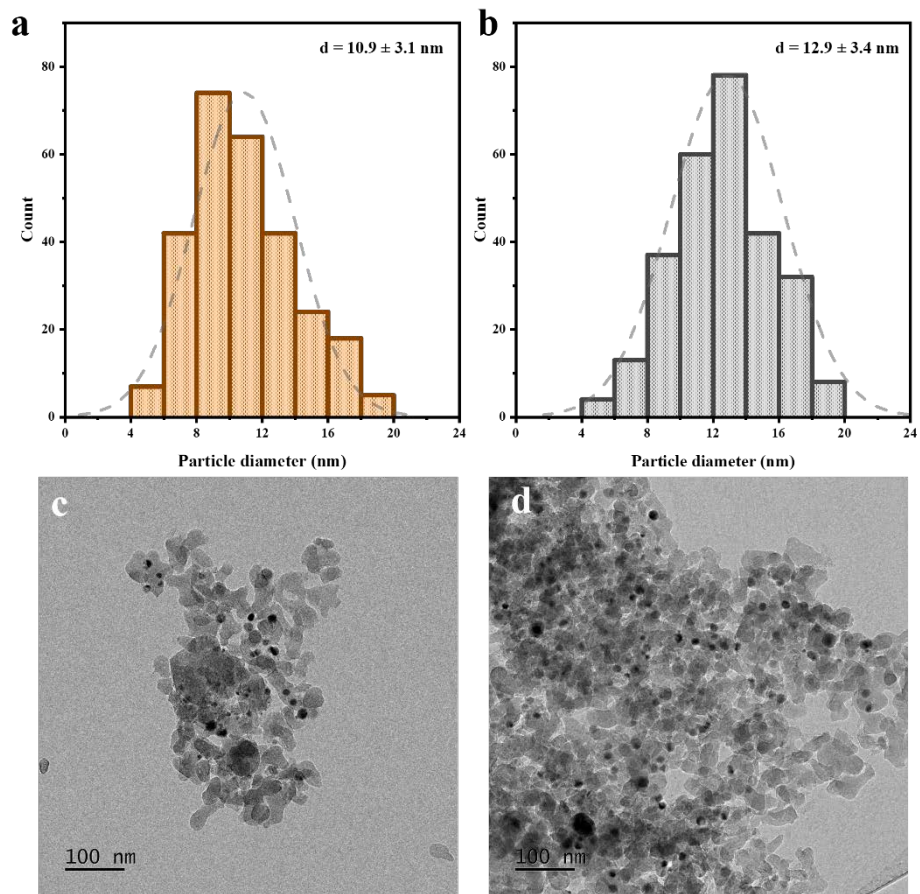


Figure S14. Typical TEM images and particle size distributions of (a, c) 0.1Pt7CuSiO₃-630R, (b, d) 0.1Pt7CuSiO₃-730R after 6 h PDH reaction.

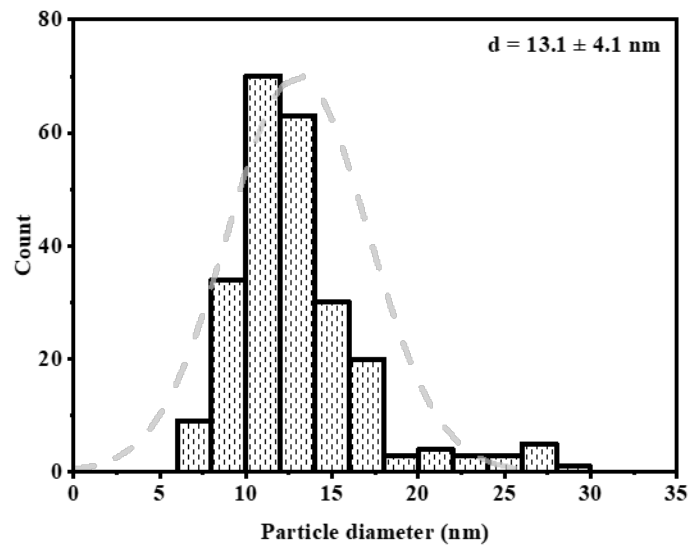
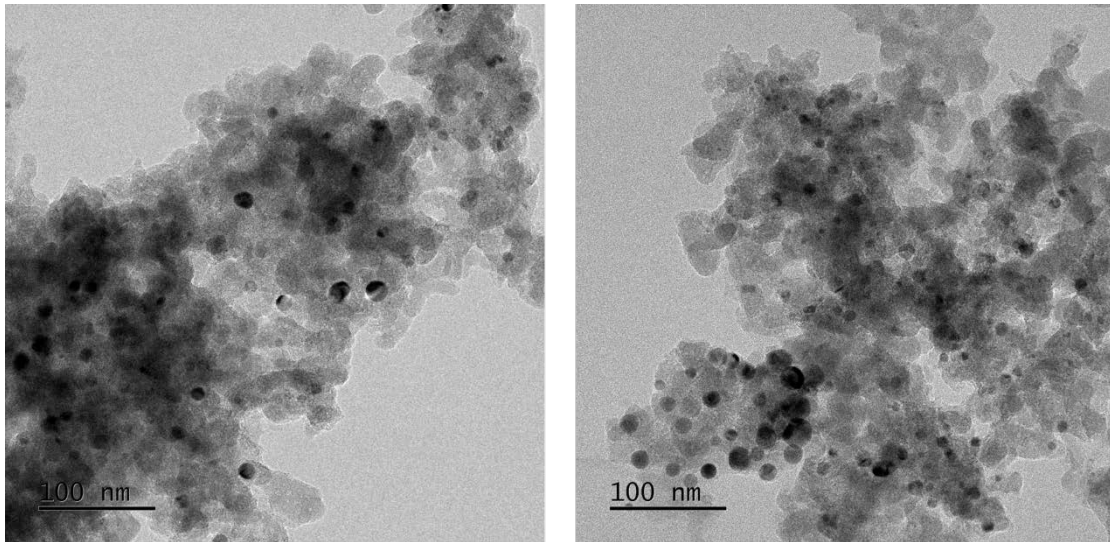


Figure S15. Typical TEM images and particle size distributions of 0.1Pt7CuSiO₃-680R after 30 h PDH reaction.

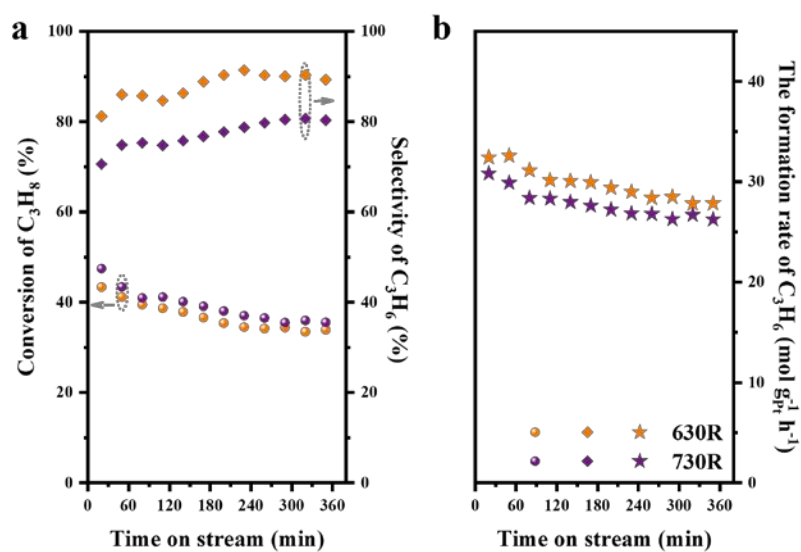


Figure S16. (a) The propane conversion, propylene selectivity and (b) the formation rate of C₃H₆ as a function of reaction time over the prepared 0.1Pt7CuSiO₃ reducing at 630, 730 °C for 1h.

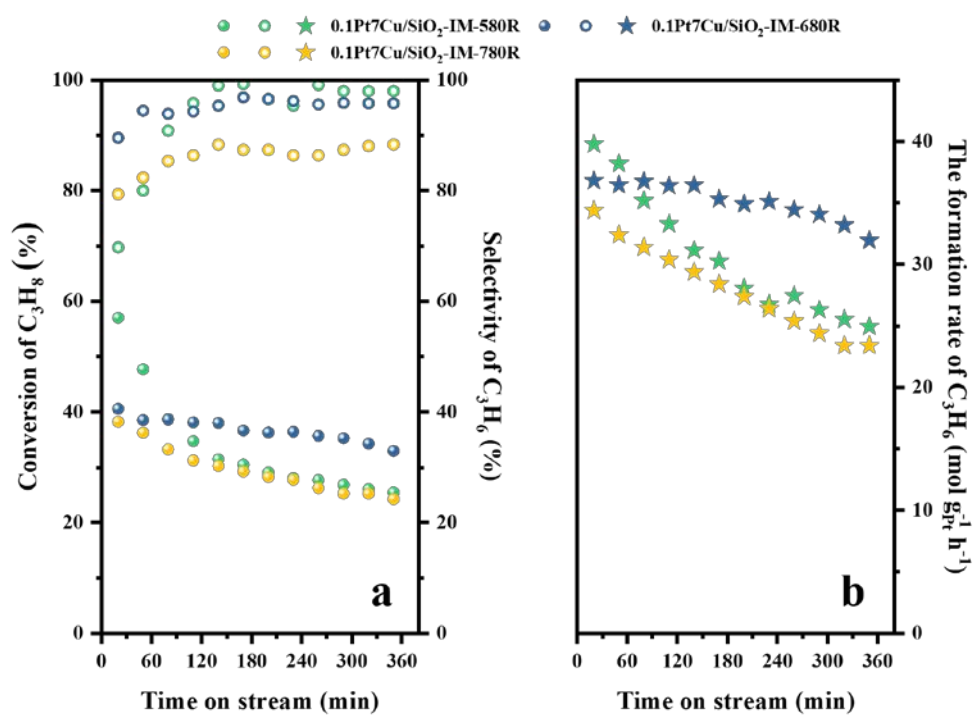


Figure S17. (a) The propane conversion, propylene selectivity and (b) the formation rate of C₃H₆ as a function of reaction time over the prepared 0.1Pt7Cu/SiO₂-IM reducing at 580, 680, 780 °C for 1h.

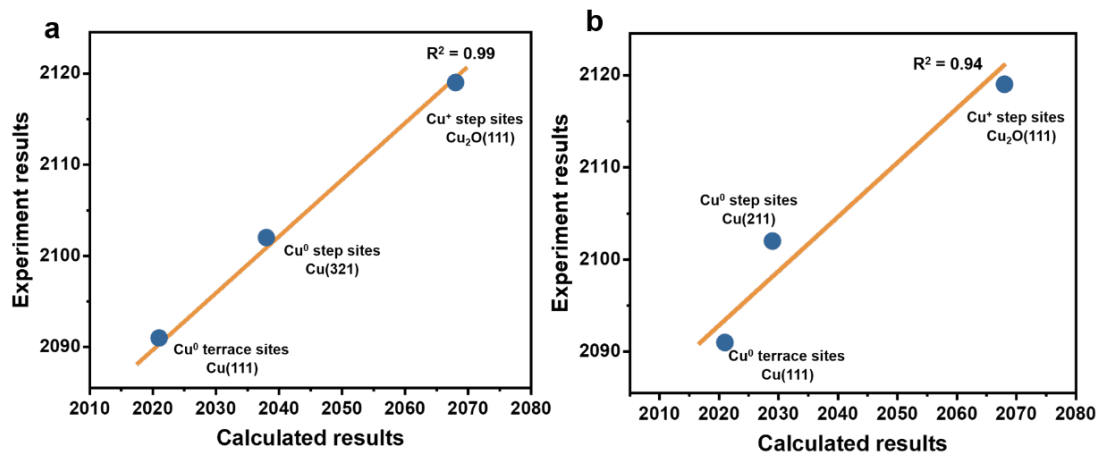


Figure S18. Calculated top adsorbed CO frequency (cm⁻¹) over on Cu⁺, Cu⁰ on step sites and Cu⁰ on terrace sites and experimentally measured frequencies.

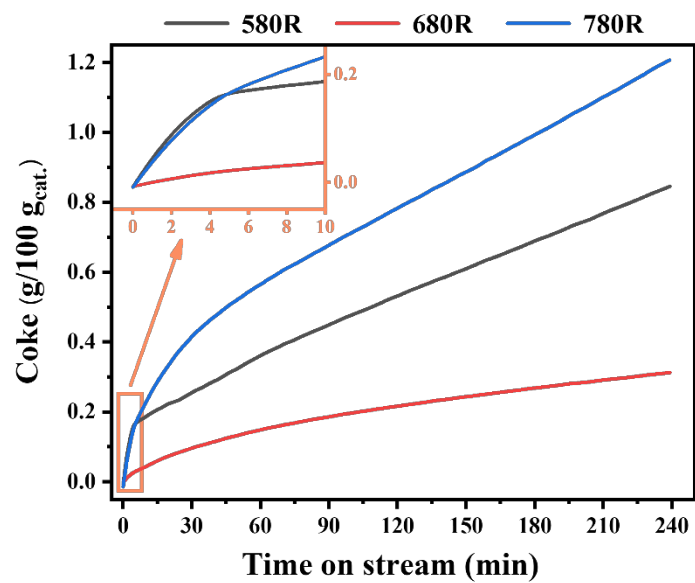


Figure S19. *In situ* Thermogravimetric (TG) test of the formation of coke for 0.1Pt7CuSiO₃ reducing at 580, 680 and 780 °C for 1h.

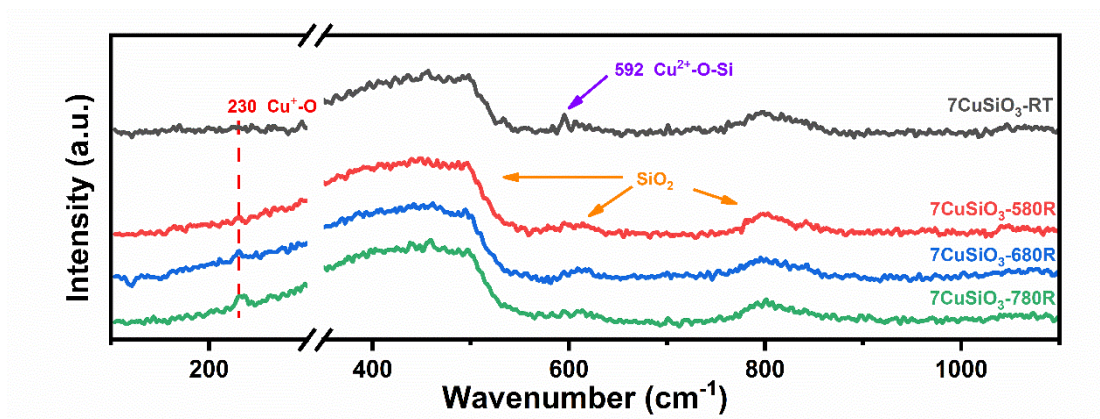


Figure S20. *In situ* Raman spectra of 7CuSiO_3 supports with different reduction temperature. (RT stands for room temperature).

As shown in Figure S20, we found the intensity of Raman peak of $\text{Cu}^+\text{-O}$ species was significant decreased compared with that of catalysts (Figure 4e), indicating that the introduction of Pt would facilitate the formation of $\text{Cu}^+\text{-O}$ species.

2.2 Supporting tables

Table S1. Physicochemical properties of the fresh and reduced catalysts

Sample	Pt loading ^a (wt.%)	Cu loading ^a (wt.%)	Cu dispersion ^b (%)	S _(Cu⁰) ^b (m ² g ⁻¹)	S _{BET} ^c (m ² g ⁻¹)	d _{pore} ^c (nm)	V _{pore} ^c (m ³ g ⁻¹)	Atomic ratio of Cu/Si (×100) ^d
0.1Pt7Cu/SiO ₂ - IM	0.1	6.9	-	-	-	-	-	7.11 (Theoretical values)
0.1Pt7Cu/SiO ₂ - IM-680R	0.1	7.1	19.9	9.03	-	-	-	-
0.1Pt7CuSiO ₃	0.1	6.8	-	-	171.1	4.84	0.230	-
0.1Pt7CuSiO ₃ - 580R	0.1	6.8	32.5	14.75	167.4	4.88	0.189	4.34
0.1Pt7CuSiO ₃ - 630R	0.1	6.8	31.7	14.39	169.3	4.89	0.187	-
0.1Pt7CuSiO ₃ - 680R	0.1	6.9	29.3	13.32	163.1	4.89	0.182	3.66
0.1Pt7CuSiO ₃ - 730R	0.1	6.9	23.7	10.79	162.9	4.92	0.179	-
0.1Pt7CuSiO ₃ - 780R	0.1	6.9	20.9	9.52	159.7	4.91	0.175	3.47

^a Determined by ICP-OES analysis.

^b Copper dispersion and surface area of Cu⁰ (S_(Cu⁰)) were determined by N₂O surface oxidation.

^c Determined by N₂ absorption-desorption analysis.

^d Determined by *quasi in situ* XPS

Table S2. The average nanoparticle size of PtCu SAA before and after 6h PDH reaction

Sample	Diameter of metallic particles in reduced sample ^a (nm)	Diameter of metallic particles in used sample ^a (nm)
0.1Pt7Cu/SiO ₂ -IM-680R	28.0	-
0.1Pt7CuSiO ₃ -580R	8.8	14.3
0.1Pt7CuSiO ₃ -630R	9.1	10.9
0.1Pt7CuSiO ₃ -680R	10.5	11.6
0.1Pt7CuSiO ₃ -730R	11.1	12.9
0.1Pt7CuSiO ₃ -780R	14.2	28.9

^a The particle size was calculated from TEM

Table S3 Calculated top adsorbed CO frequency (cm^{-1}) over on Cu^+ , Cu^0 on step sites and Cu^0 on terrace sites and experimentally measured frequencies.

Calculations		Experiments	
Slab	$\nu_{\text{C-O}}$ (cm^{-1})	Sample	$\nu_{\text{C-O}}$ (cm^{-1})
Cu(111)	2021	Cu^0 terrace sites	2091
Cu(321)	2038	Cu^0 step sites	2102
Cu(211)	2029		
$\text{Cu}_2\text{O}(111)$	2068	Cu^+ step sites	2119

The maximum error between the calculated results and the experiment results is only 3%, which is within a reasonable range of error for the calculated predictions.

Table S4. Catalytic properties of propane dehydrogenation over some representative Pt-based catalysts

NO.	Catalysts ^a	Pt (wt.%)	Temp. (°C)	WHSV (h ⁻¹)	Components (vol.%)	X _{Initial} (%)	X _{Final} (%)	S (%)	Specific activity ^b (s ⁻¹)	k _d ^c (h ⁻¹)	Ref.
1	Leached PtFe@Pt/SBA-15	0.75	600	3.48	C ₃ H ₈ =26, H ₂ =26, N ₂ =48	35	31	85	0.170	0.1360	10
2	2.5Si@0.1PtGa/Al ₂ O ₃	0.1	450	1.2	C ₃ H ₈ =2.5, H ₂ =2.5, Ar=95	21	12	90.7	0.297	0.0070	11
3	PtGa-Pb/SiO ₂	3	600	30.7	C ₃ H ₈ =8.0, H ₂ =10.2, N ₂ =81.8	30(4h)	28.4	99.6	0.38	0.0010	12
4	1Pt3Sn/CeO ₂	1	680	2.2	C ₃ H ₈ =16.7, He=83.3	45	39.5	78	0.092	0.0376	13
5	3PtSn/SiO ₂	3	500	47	C ₃ H ₈ =20, N ₂ =80	27	24	99.5	0.515	0.0527	14
6	0.04Pt0.36Zn/DeAlBEA	0.73	550	216	C ₃ H ₈ =25, He=75	18.2(75min)	17.5	99.5	1.49	0.0040	15
7	0.44Pt1Sn@MFI	0.44	450	1.7	C ₃ H ₈ =24, N ₂ =7	70	48	90	0.298	0.0143	16
8	0.28Pt/ND@G	0.28	600	1.6	C ₃ H ₈ =5, N ₂ =95	16.4	11.7	88	0.103	0.0049	17
9	PtLa/MFI	1	580	11	C ₃ H ₈ =4.6	40.0	8.0	95	0.544	0.003	18
10	Pt ⁰ Zn ^{δ+} /SiO ₂	2.9	550	75	C ₃ H ₈ =20, Ar=80	30.2	16.1	98.1	0.943	0.0271	19
11	Pt-Sn/Al ₂ O ₃	1	575	14.7	C ₃ H ₈ =20, H ₂ =16.8, He=63.2	21.1	16.6	99	0.378	0.3300	20
12	Pt1Sn1/SiO ₂	1	580	4.7	C ₃ H ₈ =16, He=84	66.2	62.5	99.4	1.674	0.0099	21
13	K-PtSn@MFI	0.40	600	29.5	C ₃ H ₈ =23.8, N ₂ =76.2	38.7	31.9	97.0	1.74	0.012	22
14	0.1Pt0.17Zn/SiO ₂ IMA	0.1	600	4	C ₃ H ₈ =14, H ₂ = 14, N ₂ = 72	48	46	96	2.269	0.0080	23
15	4.37Pt1.55Ga/SiO ₂	4.37	550	2	C ₃ H ₈ =20, Ar=80	40.7	38.5	63.5	0.016	0.0046	24
16	0.5Pt0.9Sn/Al ₂ O ₃	0.5	590	5.2	C ₃ H ₈ =16, H ₂ =20, He=64	49	39.9	97	0.607	0.0185	25
17	PtZn4@S-1-H	0.72	550	3.6	C ₃ H ₈ =25, N ₂ = 75	47.4	40.4	93.2	0.250	0.0010	26
18	0.1Pt10Cu SAA	0.1	520	4	C ₃ H ₈ =14, H ₂ = 14, N ₂ = 72	13.1	12.4	89	0.560	0.0005	27
19	1.6Cu-Pt(7.3)/SiO ₂	0.7	550	-	C ₃ H ₈ =2.5, H ₂ = 2.5, N ₂ = 95	20	13	96	0.234	0.5120	28
20	0.5Pt0.5Cu/Al ₂ O ₃	0.5	600	4	C ₃ H ₈ =14, H ₂ = 14, N ₂ = 72	44.2	40	83	0.435	0.0400	29

^a The catalysts included here are only the best performing ones from the articles considered.

^b Specific activity is defined as the moles of C₃H₆ formation per mole Pt atoms per second.

5 ^c Deactivation rate constant is calculated from $\ln[(1-X_{\text{final}})/X_{\text{final}}] = k_d \cdot t + \ln[(1-X_{\text{initial}})/X_{\text{initial}}]$

S3 References

1. X. T. Yuan, S. Chen, D. F. Cheng, L. L. Li, W. J. Zhu, D. Z. Zhong, Z. J. Zhao, J. K. Li, T. Wang and J. L. Gong, *Angew Chem Int Edit*, 2021, **60**, 15344-15347.
2. J. L. Gong, H. R. Yue, Y. J. Zhao, S. Zhao, L. Zhao, J. Lv, S. P. Wang and X. B. Ma, *J Am Chem Soc*, 2012, **134**, 13922-13925.
3. G. Kresse and J. Furthmüller, *Physical Review B*, 1996, **54**, 11169-11186.
4. J. J. Mortensen, K. Kaasbjerg, S. L. Frederiksen, J. K. Nørskov, J. P. Sethna and K. W. Jacobsen, *Phys Rev Lett*, 2005, **95**.
5. J. Wellendorff, K. T. Lundgaard, A. Mogelhoj, V. Petzold, D. D. Landis, J. K. Nørskov, T. Bligaard and K. W. Jacobsen, *Physical Review B*, 2012, **85**.
6. P. E. Blöchl, *Physical Review B*, 1994, **50**, 17953-17979.
7. L. Wang, T. Maxisch and G. Ceder, *Physical Review B*, 2006, **73**, 195107.
8. Y. F. Zhu, X. Kong, B. Peng, L. P. Li, Z. Fang and Y. L. Zhu, *Catal Sci Technol*, 2020, **10**, 7323-7330.
15. 9. S. H. Wang, K. Feng, D. K. Zhang, D. R. Yang, M. Q. Xiao, C. C. Zhang, L. He, B. H. Yan, G. A. Ozin and W. Sun, *Adv Sci*, 2022, **9**.
10. W. T. Cai, R. T. Mu, S. J. Zha, G. D. Sun, S. Chen, Z. J. Zhao, H. Li, H. Tian, Y. Tang, F. Tao, L. Zeng and J. L. Gong, *Sci Adv*, 2018, **4**.
11. P. Wang, J. Yao, Q. Jiang, X. Gao, D. Lin, H. Yang, L. Wu, Y. Tang and L. Tan, *Applied Catalysis B: Environmental*, 2022, **300**, 120731.
20. 12. Y. Nakaya, J. Hirayama, S. Yamazoe, K.-i. Shimizu and S. Furukawa, *Nat Commun*, 2020, **11**, 2838.
13. H. F. Xiong, S. Lin, J. Goetze, P. Pletcher, H. Guo, L. Kovarik, K. Artyushkova, B. M. Weckhuysen and A. K. Datye, *Angew Chem Int Edit*, 2017, **56**, 8986-8991.
25. 14. L. D. Deng, H. Miura, T. Shishido, Z. Wang, S. Hosokawa, K. Teramura and T. Tanaka, *J Catal*, 2018, **365**, 277-291.
15. L. Qi, M. Babucci, Y. Zhang, A. Lund, L. Liu, J. Li, Y. Chen, A. S. Hoffman, S. R. Bare, Y. Han, B. C. Gates and A. T. Bell, *J Am Chem Soc*, 2021, **143**, 21364-21378.
16. L. C. Liu, M. Lopez-Haro, C. W. Lopes, C. G. Li, P. Concepcion, L. Simonelli, J. J. Calvino and A. Corma, *Nat Mater*, 2019, **18**, 866-+.
30. 17. J. Liu, Y. Y. Yue, H. Y. Liu, Z. J. Da, C. C. Liu, A. Z. Ma, J. F. Rong, D. S. Su, X. J. Bao and H. D. Zheng, *Acs Catal*, 2017, **7**, 3349-3355.
18. R. Ryoo, J. Kim, C. Jo, S. W. Han, J.-C. Kim, H. Park, J. Han, H. S. Shin and J. W. Shin, *Nature*, 2020, **585**, 221-224.
35. 19. L. Rochlitz, K. Searles, J. Alfke, D. Zemlyanov, O. V. Safonova and C. Coperet, *Chem Sci*, 2020, **11**, 1549-1555.
20. H. Z. Wang, L. L. Sun, Z. J. Sui, Y. A. Zhu, G. H. Ye, D. Chen, X. G. Zhou and W. K. Yuan, *Ind Eng Chem Res*, 2018, **57**, 8647-8654.
21. A. H. Motagamwala, R. Almallahi, J. Wortman, V. O. Igenegbai and S. Linic, *Science*, 2021, **373**, 217-+.
40. 22. L. Liu, M. Lopez-Haro, C. W. Lopes, S. Rojas-Buzo, P. Concepcion, R. Manzorro, L. Simonelli, A. Sattler, P. Serna, J. J. Calvino and A. Corma, *Nat Catal*, 2020, **3**, 628-638.
23. S. Chen, Z. J. Zhao, R. T. Mu, X. Chang, J. Luo, S. C. Purdy, A. J. Kropf, G. D. Sun, C. L. Pei,

- J. T. Miller, X. H. Zhou, E. Vovk, Y. Yang and J. L. Gong, *Chem-US*, 2021, **7**, 387-405.
24. K. Searles, K. W. Chan, J. A. M. Burak, D. Zemlyanov, O. Safonova and C. Coperet, *J Am Chem Soc*, 2018, **140**, 11674-11679.
25. E. J. Jang, J. Lee, H. Y. Jeong and J. H. Kwak, *Appl Catal a-Gen*, 2019, **572**, 1-8.
- 5 26. Q. M. Sun, N. Wang, Q. Y. Fan, L. Zeng, A. Mayoral, S. Miao, R. O. Yang, Z. Jiang, W. Zhou, J. C. Zhang, T. J. Zhang, J. Xu, P. Zhang, J. Cheng, D. C. Yang, R. Jia, L. Li, Q. H. Zhang, Y. Wang, O. Terasaki and J. H. Yu, *Angew Chem Int Edit*, 2020, **59**, 19450-19459.
27. G. Sun, Z. J. Zhao, R. Mu, S. Zha, L. Li, S. Chen, K. Zang, J. Luo, Z. Li, S. C. Purdy, A. J. Kropf, J. T. Miller, L. Zeng and J. Gong, *Nat Commun*, 2018, **9**, 4454.
- 10 28. Z. Ma, Z. Wu and J. T. Miller, *Catalysis, Structure & Reactivity*, 2017, **3**, 43-53.
29. Z. P. Han, S. R. Li, F. Jiang, T. Wang, X. B. Ma and J. L. Gong, *Nanoscale*, 2014, **6**, 10000-10008.